General Disclaimer

One or more of the Following Statements may affect this Document

- This document has been reproduced from the best copy furnished by the organizational source. It is being released in the interest of making available as much information as possible.

- This document may contain data, which exceeds the sheet parameters. It was furnished in this condition by the organizational source and is the best copy available.

- This document may contain tone-on-tone or color graphs, charts and/or pictures, which have been reproduced in black and white.

- This document is paginated as submitted by the original source.

- Portions of this document are not fully legible due to the historical nature of some of the material. However, it is the best reproduction available from the original submission.

Final Report for Contract NASW-3741

of a

FEASIBILITY STUDY TO CONDUCT WINDBLOWN SEDIMENT

EXPERIMENTS ABOARD A SPACE STATION

by

Ronald Greeley
Department of Geology
Arizona State University
Tempe, Arizona 85287

and

James D. Iversen
Department of Aerospace Engineering
Iowa State University
Ames, Iowa 50010

submitted to: National Aeronautics and Space Administration

Attn: Dr. Ken Frost
Program Manager
Space Station

submitted 30 August 1983
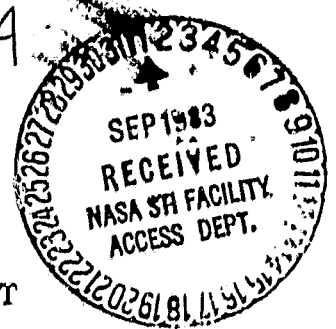
1.0 Introduction

It is estimated that more than 500×10^6 metric tons of dust are transported annually by the wind (Peterson and Junge, 1971). Dust storms reduce visibility on highways and are responsible for loss of life and property through many accidents each year. Atmospheric dust, whether raised by winds or injected into the atmosphere by volcanic processes, can also have a significant effect on temperature. Thus, windborne particles can have a direct effect on the climate. In addition, windblown sands cause abrasion and erosion of natural and manufactured objects and encroach upon cultivated areas, turning productive land to desert--a process termed desertification. The problem of desertification is enormous and is recognized on all inhabited continents of Earth. Agricultural land damaged by wind erosion in the United States alone varies from 400 to 6,000 km^2 per year (Kimberlin et al., 1977).

The key to understanding problems associated with windblown sediments, including those aspects of desertification dealing with wind processes, is knowledge of the physics of windblown particles.

Many parameters, such as grain size and wind speed, must be considered in assessing the entrainment and transport of windblown grains. Beginning with Bagnold's (1941) research in the 1930's, numerous investigators have used wind tunnels to analyze particle entrainment. Wind tunnels have the advantage that individual parameters can be closely controlled and isolated for study and analysis. Gravity is one of the most critical parameters in the analysis of windblown sediment movement; however, there is no effective means for isolating and assessing its effect during experiments conducted on Earth. Hence, a space station would afford an opportunity to conduct experiments in zero-gravity and variable-gravity environments. Such experiments would enable not only this parameter to be assessed, but through its elimination as a

factor in the experiments, other critical parameters could be evaluated as
well.

The objective of this feasibility study was to determine if a suitable
apparatus could be designed to analyze aeolian processes for operation in
space and to assess the feasibility of conducting meaningful experiments to
address.key aspects of aeolian processes. To meet this objective a prototype
apparatus was fabricated and some limited experiments were run to determine
its suitability for this application.

2.0 Potential Experiments in the Space Station Environment

We envisage at least three general types of experiments that could be
carried out aboard a space station: threshold studies, swirl (dust devil)
experiments, and analyses of windblown particle trajectories. In this section
we consider how experiments in a zero-g environment could advance knowledge of
aeolian processes.

2.1 Threshold Experiments

Threshold (u_{*t}) defines the minimum winds required to initiate particle
motion and is the fundamental factor in aeolian processes. In the
determination of a general expression of the threshold wind speeds for small
(~ sub-millimeter) particles, the effect of aerodynamic forces tending to
dislodge a particle from a bed of loose granular material is equated to the
effect of opposing forces, namely the particle weight (W) and interparticle
cohesion (I). The relative magnitudes of these forces have been deduced only
approximately from wind tunnel tests of threshold speed (Iversen et al., 1976;
Greeley et al., 1980a; Iversen and White, 1982).

The elimination of particle weight in the threshold force equation —as
could be accomplished by conducting experiments in a weightless environment—
would enable a more accurate assessment of the other factors. The equation of

Table 1. Nomenclature

a_p pressure differences proportionality coefficient

C_D drag coefficient

C_L lift coefficient

c_τ surface stress coefficient for a vortex

D aerodynamic drag

D_p particle diameter

g gravity

I cohesive force

K central layer speed coefficient (Eq. 8)

L lift

M moment

R_* particle friction Reynolds number

R_i inner drum radius

R_o outer drum radius

r radial coordinate, carrousel wind tunnel

r_o characteristic vortex radius

r_1 radius at boundary between central layer and outer boundary layer

r_2 radius at boundary between central layer and inner boundary layer

U wind speed

u_{*i} inner drum surface friction speed

u_{*o} outer drum surface friction speed

u_{*t} threshold friction speed

V_r wind speed relative to particle

W particle weight

θ angular coordinate

ν kinematic viscosity

ρ atmospheric density

ρ_p particle density

σ_I tensile stress due to interparticle cohesion

ω inner drum rotational speed

ω_o rotational angular velocity of a vortex generator

equilibrium for a small particle at threshold is

$$Da + Lb + M = Ic + Wb \tag{1}$$

Where D, L, and M are aerodynamic drag, lift, and moment, respectively, W is particle weight, I is cohesive force (see Table 1), and a, b, and c are distances from lines of action of the forces to the overturning point. Figure 1 illustrates the force system acting on the particle at rest. Elimination of the weight term would aid in the determination of the form and magnitude of the cohesive force term at the moment of threshold.

The equilibrium of the forces at incipient motion can be used to express an equation for threshold. For values of particle friction Reynolds number, R_*, between 0.3 and 10 (normal range for sand on Earth), the resulting semi-empirical equation (Iversen and White, 1982) is

$$u_{*t}^2 = 0.0166 \frac{\rho_p g D_p}{\rho} \left[1 + \frac{0.006}{\rho_p g D_p^{2.5}} \right] \div [1.928 R_*^{0.092} - 1] \tag{2}$$

With the elimination of the weight term, the equation becomes

$$u_{*t}^2 = 0.0001 \; [1.928 R_*^{0.092} - 1] \div \rho D_p^{1.5} \tag{3}$$

Experimental data for threshold at one Earth atmosphere are shown in Figures 2 and 3. The expectation of threshold at zero-g is shown in Figure 4.

2.2 Swirl Threshold Experiments

Cyclonic atmospheric motions, or "dust devils", are effective in raising large quantities of very fine-grained particles in local settings such as cultivated fields. Such motion often occurs in otherwise calm atmospheric conditions and may be responsible for the onset of some major dust storms. The physics of particle entrainment by dust devils is virtually unknown, although some preliminary small-scale experiments have been conducted previously (Greeley et al., 1981). A semi-empirical equation was derived from these experiments

$$(r_o\omega_o)^2 = \left[\frac{1}{a_p + c_\tau}\right]\left[\frac{\rho_p g D_p}{\rho}\right]\left[1 + \frac{\sigma_I}{\rho_p g D_p}\right] \tag{4}$$

where $r_o\omega_o$ is a representation of maximum tangential speed within the dust-devil vortex. If the weight force is eliminated as could be accomplished in a zero-g environment, the result is

$$(r_o\omega_o)^2 = \frac{\sigma_I}{\rho(a_p + c_\tau)} \tag{5}$$

Elimination of the weight as a force simplifies the equation and would allow more accurate measurements of aerodynamic and interparticle forces. The effect of the difference between Equations 4 and 5 is illustrated in Figure 5.

2.3 Particle Trajectories

Once particles are airborne, the forces acting on individual grains in their trajectories are the particle weight and the aerodynamic lift and drag. The two-dimensional equations of motion of a particle moving through the air can be written as

$$\frac{4}{3}\frac{\rho_p}{\rho} D_p\ddot{x} = \dot{y}V_r C_L - (\dot{x} - u) V_r C_D$$

$$\frac{4}{3}\frac{\rho_p}{\rho} D_p\ddot{y} = -(\dot{x} - u)V_r C_L - \dot{y}V_r C_D - \left|\frac{4\rho_p g D_p}{3\rho}\right| \tag{6}$$

$$V_r^2 = (\dot{x} - u)^2 + \dot{y}^2$$

The dotted line surrounds the weight factor. Experimental and calculated trajectories for one-g conditions are illustrated in Figure 6. With the elimination of the weight factor under zero-g, the only forces remaining are aerodynamic. Thus, experiments conducted in zero-g would enable aerodynamic lift and drag to be assessed.

3.0 Carrousel Wind Tunnel (CWT) Design

Boundary-layer wind tunnels appropriate for investigations of aeolian processes typically exceed 10 m in length (e.g. Bagnold, 1941; Greeley et al., 1981). Because of the probable size constraints in an orbital laboratory, we evaluated various wind tunnel designs that would provide a compact apparatus and which would be suitable for conducting the types of experiments outlined in Section 2. Based on these considerations, we designed a wind tunnel not previously used in aeolian studies. The type of wind tunnel we propose consists of two concentric rotating drums (Fig. 7). The space between the two drums comprises the wind tunnel test section. Differential rates of rotation of the two drums would provide a wind velocity with respect to either drum surface. Rotation of the outer drum provides a "pseudo" gravity ("pseudo" in the sense that a gravity force acts on the particle only when it is resting on the outer drum surface).

In order to test the concept of this wind tunnel design, a 1/3 scale model Carrousel Wind Tunnel (CWT) was constructed and calibrated (Figs. 8-10). In this prototype, only the inner drum rotates, whereas in the final configuration, both drums would rotate. The drum walls are plexiglass to allow observation of the test section. The inner drum is 712 mm in diameter and 258 mm wide and is spun around a horizontal axis at a constant speed of 515 rpm (53.9 rad/s), which gives a drum-surface speed of 19.2 m/s (63 ft/s). The outer drum is 1062 mm in diameter and 263 mm wide. In a full-scale model, both drums would rotate at controllable, variable speeds. The outer drum is sealed along its periphery, but there is a small gap between the sides of the inner drum and the outer drum. It is assumed that a zero-g environment would be available on board a space station, and that atmospheric pressure environments over the range of 1 bar down to low (~1 mb) pressure would be available.

4.0 Prototype Testing and Experimental Comparisons

A series of experiments was conducted to determine the boundary layer properties of the prototype CWT. Taylor (1935) hypothesized nearly potential (inviscid) flow for the turbulent flow between concentric rotating cylinders and noted that boundary layers near the outer and inner walls should be governed by Prandtl's mixing-length theory. In CWT it is important that the mixing-length theory govern the boundary-layer flow adjacent to the curved cylinder wall surfaces because the same theory governs the flow adjacent to a plane surface and would be comparable to natural conditions and to conditions used in previous threshold experiments (Greeley et al., 1976, 1980b; Iversen et al., 1976). Experiments were performed in CWT to ascertain if these assumptions are correct and if Taylor's hypothesis is valid. For cases in which only the inner cylinder rotates (as in the prototype CWT) and assuming that the surfaces of the cylinder walls are aerodynamically smooth, the following equations for the flow between two infinitely long cylinders (Fig. 11) can be derived:

inner layer (Prandtl boundary layer)

$$U = R_1\omega - u_{*i} \{2.5 \ln [(r - R_1)u_{*i}/\nu] + 5.5\}$$

$$\text{for } R_1/R_o + (\nu/u_{*i}R_o)e^{0.4R_1\omega/u_{*i}} \tag{7}$$

$$< r/R_o < r_2/R_o$$

central layer (potential inviscid layer)

$$U = KR_1\omega(R_o + R_1)/4r$$

$$\text{for } r_2/R_o < r/R_o < r_1/R_o \tag{8}$$

outer layer (Prandtl boundary layer)

$$U = u_{*o} \{5.5 + 2.5 \ln [(1 - \frac{r}{R_o}) R_o\, u_{*o}/\nu]\}$$

$$\text{for } r_1/R_o < r/R_o \tag{9}$$

$$< 1 - 0.1108/(R_o\, u_{*o}/\nu)$$

To determine the flow characteristics in the CWT, wind velocity profiles were obtained in the prototype using a TSI model 1010 hot-wire probe anemometer at four positions in the tunnel: 17.5, 39.5, 77.5, and 126.5 mm from the side of the drum and within about 5 mm from the inner drum to about 5 mm from the outer drum. The velocities and distances were non-dimensionalized by dividing the wind velocity by the inner drum rim speed $(U/R_i\omega)$ and the distance by the outer drum radius (r/R_o).

The theoretical Eqs. 7, 8, 9 were then matched to the experimental data by first fitting the data in the central layer to Eq. 8. Then the values of r_1, r_2, u_{*i}, u_{*o} were calculated by trial and error by matching values of speed U and slope dU/dr at the inner layer – central layer and outer layer – central layer boundaries. The results are shown in Table 2 and Figures 11-14.

Table 2. Speed Profile Characteristics

Station No. (mm)	r_1/R_o	r_2/R_o	u_{*i} (cm/s)	u_{*o} (cm/s)	K	$\dfrac{U}{K_i\omega}$ @ $\dfrac{R_i + R_o}{2}$
17.5	0.9016	0.7915	46.9	29.4	0.316	0.378
39.5	0.9015	0.7941	47.2	29.2	0.313	0.373
77.5	0.9015	0.7942	47.2	29.1	0.313	0.375
126.5	0.9016	0.7911	46.9	29.4	0.317	0.379

Both the data in the table and in the figures show that the flow is quite uniform across the breadth of the wind tunnel cross-section. Figure 15 is a comparison of theoretical velocity distributions. In Figures 11 and 13, the central and outer theoretical layers give remarkably close fits to the data,

and in Figure 14 the central and inner theoretical profile layers fit the data quite well. The primary reason for the slight discrepancy between theory and experiment, especially for the inner layer in Figures 11-13, is the existence of secondary flows in the wind tunnel cross-section which are not taken into account in the theory.

These experiments show that Taylor's hypothesis appears to be correct. The results also show that surface friction speeds can be predicted a priori with some degree of accuracy, facilitating the design of CWT and enabling a reasonable experimental matrix to be developed.

The velocity profile data of Figures 11-15 show that the desired two-dimensionality of the flow in the carrousel is very nearly realized over most of the cross-section. The variation of measured speed across the cross-section width is illustrated in Figure 16 for three radial positions and shows that secondary flows are concentrated near the inner (rotating) cylinder. Turbulence levels of 6% to 10% were measured within the inner and outer boundaries, which are within levels to be expected in normal, flat-plate boundary layers developed within conventional atmospheric wind tunnels.

From these calibration experiments and flow-field determinations, we conclude that the CWT boundary layer environment is appropriate for experiments dealing with threshold and particle trajectories.

5.0 Particle-Trajectory Calculations

In order to assess the suitability of CWT in the analysis of the trajectories of windblown particles, a series of calculations was conducted comparing cases for one-g with those of zero-g. The equations of motion for an airborne particle, assuming no lift force, are (in a polar coordinate system):

$$\ddot{r} - r\,\dot{\theta}^2 - g\,\cos\theta + \left(\frac{3\rho C_D \dot{r}}{4\rho_p D_p}\right) V_r = 0$$

$$r\,\ddot{\theta} + 2\,\dot{r}\,\dot{\theta} + g\,\sin\theta - \left(\frac{3\rho C_D}{4\rho_p D_p}\right) [U(r) - r\,\dot{\theta}]\, V_r = 0 \qquad (10)$$

$$V_r = \{\dot{r}^2 + [U(r) - r\,\dot{\theta}]^2\}^{1/2}$$

Equations 10 were solved for several example cases. The drag coefficient, C_D, is a function of Reynolds number, assuming a spherical particle (White et al., 1975). Figure 17 illustrates particle trajectories in CWT for a zero-g vacuum for 5 different initial radial velocities. The coordinate system is fixed to the particle launch point and rotates with the outer cylinder. In inertial space the trajectories are straight lines, but relative to an observer standing on the launch point of the rotating outer drum, as plotted, the trajectories are curved. For comparison, a particle trajectory is shown in Figure 18, also for zero-g but in an environment of one atmosphere air. The initial inward radial velocity of the particle is assumed to be equal to the surface friction speed of the outer cylinder (32.6 cm/s). The assumed wind speed profile for the calculation is shown in Figure 19. The trajectories in Figures 20 and 21 were calculated in order to compare trajectories with and without the effect of gravity. The same velocity profile as in Figure 19 was used to determine the particle trajectory on the Earth's surface and is shown in Figure 20. Also shown in Figure 20 is the trajectory of Figure 18, plotted in a rectangular coordinate system. The effect of gravity is to lower the trajectory height by a factor of about one-third. Since the only force acting on the particle in CWT is aerodynamic, the significant difference between the two trajectories should enable much more accurate determination of the aerodynamic forces (drag and lift) than is

possible in an Earth-based facility. This difference can also be shown by calculating the particle trajectory in the carrousel when it is positioned on the Earth's surface, as in the prototype tests. For the trajectory of Figure 21, the particle is initially located at the lowest position of the outer cylinder and gravitational attraction is in the negative vertical direction. Again the trajectory peak (3 mm) is about one-third lower than that in Figure 18 (5 mm).

We conclude that CWT could yield significant data on the trajectories of windblown particles.

6.0 Summary and Conclusions

A wind tunnel apparatus was designed as appropriate for use in an orbital space station. A 1/3 scale prototype system was fabricated and its flow characteristics were assessed. Preliminary results show uniform flow and boundary layer properties that are in agreement with theory. Experiments were conducted in the prototype to determine the feasibility of studying various aeolian processes and the results were compared with various numerical analyses. Several types of experiments appear to be feasible utilizing the proposed apparatus:

Threshold Experiments under Varying Gravity

Aeolian threshold experiments for a wide range of atmospheric pressures (0.004 to 30 atmospheres) have been conducted previously (Iversen et al., 1976; Greeley et al., 1976, 1980a,b). All of these experiments have been conducted under conditions of Earth's gravity. It would be extremely valuable to extend the matrix of experiments to include values of artificial gravity above and below that experienced on Earth. This could be accomplished in CWT by placing a bed of particles on the inner surface of the outer drum and rotating the outer drum at different rotational speeds. The rotating outer drum provides an

acceleration directed radially outwards, normal to the surface, thus creating artificial gravity. While rotating the outer drum at a constant rate to maintain a constant value of artificial gravity, the inner drum speed can be changed to increase the value of outer-drum wind-friction speed until the top layer of particles leaves the surface at which point the threshold wind friction speed can be ascertained.

Threshold Experiments for Zero Gravity Conditions

Zero-gravity threshold experiments are valuable because of the elimination of the weight term in Equation (1). Such experiments would enable cohesion forces to be assessed, as discussed in section 2. These experiments would be conducted by rotating only the inner drum, accelerating its speed until threshold is reached.

Swirl Threshold Experiments

Threshold experiments and particle motion in the zero-g environment would also be carried out in a dust-devil simulator, an apparatus used in previous experiments (Greeley et al., 1981). The same advantages are found in these experiments as for threshold experiments, i.e., forces of cohesion and atmospheric lift and drag can be separated from the effects of particle weight and thus can be determined much more accurately.

Experiments to Study Particle Trajectories

Analysis of particle trajectories in a zero-g environment would enable the determination of the aerodynamic forces on windblown particles using high-speed motion picture obtained during the experiments. The lift and drag forces would be determined by measuring particle accelerations, particle speeds, and wind speeds, and applying Equation 6 to the results.

Analyses of Bed-Forms

Small bedforms, such as ripples, are of great interest in aeolian phenomena. Because the physics of ripple formation are poorly understood, it

is not known if ripples would form in the space station carrousel, although it is expected that ripples would form because the particle trajectories relative to the bed would be similar to those on Earth (Fig. 20).

By rotating the inner drum at a faster rotational speed than the outer drum, a wind velocity profile could be generated which would cause saltation from a bed of particles situated on the inner surface of the outer drum. By observation under a variety of rotational rates and rate differences, experiments in the controlled environment of the carrousel could increase understanding of the physics involved in ripple formation.

In conclusion, results from this feasibility study demonstrate that a wind tunnel of the carrousel design could be fabricated to operate in a space station environment and that experiments could be conducted which would yield significant results contributing to the understanding of aeolian processes.

Acknowledgements

REFERENCES CITED

Bagnold, R.A., 1941. The Physics of Blown Sand and Desert Dunes: Methuen, London, 265 pp.

Greeley, R., B.R. White, R.N. Leach, J.D. Iversen, and J.B. Pollack, 1976. Mars: Wind friction speeds for particle movement: Geophys. Res. Lett. 3, 417-420.

Greeley, R., R. Leach, B.R. White, J.D. Iversen, and J.B. Pollack, 1980a. Threshold windspeeds for sand on Mars: Wind tunnel simulations: Geophys. Res. Lett. 7, 121-124.

Greeley, R., B.R. White, R. Leach, R. Leonard, J.B. Pollack, and J.D. Iversen, 1980b. Venus aeolian processes: saltation studies and the venusian wind tunnel: NASA TM-82385, 275-277.

Greeley, R., B.R. White, J.B. Pollack, J.D. Iversen, and R.N. Leach, 1981. Dust storms on Mars: Considerations and simulations: in T. Pewe, ed., Desert Dust: Origin, Characteristics, and Effect on Man. Geol. Soc. Am. Spec. Pap. 186, 101-121.

Iversen, J.D. and B.R. White, 1982. Saltation threshold on Earth, Mars, and Venus: Sedimentology 29, 111-119.

Iversen, J.D., J.B. Pollack, R. Greeley, and B.R. White, 1976. Saltation threshold on Mars: the effect of interparticle force, surface roughness, and low atmospheric density: Icarus 29, 381-393.

Kimberlin, L.W., A.R. Hidlebaugh, and A.R. Grunewald, 1977. The potential wind erosion problem in the United States: Trans. Am. Soc. Agric. Eng. 20, 873-879.

Peterson, S.T., and C.E. Junge, 1971. Sources of particulate matter in the atmosphere: in Man's Impact on the Climate, MIT Press, Cambridge, 310-320.

Taylor, G.I., 1935. Distribution of velocity and temperature between concentric rotating cylinders: Proc. Royal Soc. London, Series A 151, 494-512.

White, B.R., and J.C. Schulz, 1977. Magnus effect on saltation: Jour. Fluid Mech. 81, 497-512.

White, B.R., J.D. Iversen, R. Greeley and J.B. Pollack, 1975. Particle motion in atmospheric boundary layers of Mars and Earth: NASA TMX-62463, 200 pp.

FIGURE CAPTIONS

Fig. 1. Forces on a particle at the threshold of motion (here idealized as a sphere and resting on a bed of like particles) include aerodynamic lift (L), drag (D),and moment (M), weight (W) and interparticle or cohesive force (I_p). The only force remaining to resist motion at zero gravity is the cohesive force I_p. Isolation of this force would permit much more accurate evaluation of its effect in aeolian processes.

Fig. 2. Experimental data for threshold at the Earth's surface show that the interparticle force I_p is the dominant resisting force for small particles and the weight is dominant for large particles, resulting in an "optimum" particle diameter for minimum threshold (from Iversen et al., 1976).

Fig. 3. The difference between the two curves on the left side of the figure illustrates the approximate relative magnitude of the cohesive force compared to weight for smaller particles.

Fig. 4. Threshold friction speed versus particle diameter on Earth and the expectation of threshold under zero-g; large particles could be moved more easily.

Fig. 5. Swirl (dust-devil) threshold speed on Earth (one-gravity) compared to values expected at zero-g; as for the boundary-layer threshold, the swirl threshold speed would decrease for larger particles (right-hand-side).

Fig. 6. Trajectories of windblown particles; the solid line is an experimental trajectory at the earth's surface, the broken lines are calculated (from White and Schultz, 1977). Zero-gravity experiments will have two major advantages: (1) the threshold speeds for larger particles are much lower, thus much lower wind and particle speeds are possible, and (2) elimination of the force due to particle weight means the aerodynamic forces can be measured (analysis of motion pictures) much more accurately than on Earth. Results would improve understanding of particle physics, having important applications to problems involving blowing sand, dust, soil, and snow.

Fig. 7. Isometric representation of the carrousel drums.

Fig. 8. Photograph of prototype Carrousel Wind Tunnel (CWT).

Fig. 9. Dimensions of the inner and outer concentric drums of the prototype CWT.

Fig. 10. Close-up photograph of the hot-wire anemometer probe mechanism used to determine the flow properties of the prototype CWT.

Fig. 11. Wind velocity profile data at station 17.5 mm from tunnel side wall.

Fig. 12. Wind velocity profile data at station 39.5 mm from tunnel side wall.

FIGURE 1

u_{*_t} VS $\sqrt{D_P}$

	MATERIAL	DENSITY ~ gm/cm^3	DIAMETER ~ cm
◖	INSTANT TEA	0.21	719
◿	SILICA GEL	0.89	17; 169
□	NUT SHELL	1.1	40 TO 359
◊	CLOVER SEED	1.3	1290'
◇	SUGAR	1.59	393
◺	GLASS	2.42	31 TO 48
○	GLASS	2.5	38 TO 586
◭	SAND	2.65	526
◗	ALUMINUM	2.7	36 TO 204
△	GLASS	3.99	55 TO 519
⌂	COPPER OXIDE	6.0	10
▽	BRONZE	7.8	616
◇	COPPER	8.94	12; 37
◇	LEAD	11.35	8; 720

AIR DENSITY ~ ρ = 0.001226 gm/cm^3
KINEMATIC VISC. ~ ν = 0.1464 cm^2/sec

THRESHOLD FRICTION SPEED ~ u_{*_t} ~ cm/sec

(DIAMETER)$^{1/2}$ ~ $\sqrt{D_P}$ ~ (MICRONS)$^{1/2}$

FIGURE 2

FIGURE 3

On the plot, the following annotations appear:

$$A = u_{*_t}(\rho/\rho_p g D_p)^{1/2}$$

$$B = u_{*_t} D_p/\nu$$

$$k = 0.006 \text{ gm cm}^{0.5} \text{ s}^{-2}$$

REAL PARTICLES (SAND, 1 ATMOS.)

$$0.243[1 - 0.0858 \, e^{-0.0617(B - 10)}]^{2/3} B^{1/3} \qquad 10 \leq B$$

COHESIONLESS PARTICLES

$$0.255[B/(1.928 B^{0.092} - 1)]^{1/3}, \quad 0.03 \leq B \leq 10$$

	D_p (µm)	ρ_p/ρ
LOW DENSITY WT o	37 to 673	900 to 350,000
ISU WIND TUNNEL ●	12 to 1290	173 to 9,400

Axis labels:

PARTICLE FRICTION REYNOLDS NO. B

DIMENSIONLESS COHESIONLESS THRESHOLD FRICTION SPEED

$$[A^2 B/(1 + k/\rho_p g D_p^{2.5})]^{1/3}$$

THRESHOLD FRICTION SPEED CM/S

PARTICLE DIAMETER   MICRONS

EARTH'S SURFACE

ZERO GRAVITY

FIGURE 4

FIGURE 5

FIGURE 6

FIGURE 7

FIGURE 8

258

263

1062
DIA.

712 DIA.

ALL DIMENSIONS IN MM.

FIGURE 9

ORIGINAL PAGE
COLOR PHOTOGRAPH

FIGURE 10

VELOCITY PROFILE AT STATION 17.5

R1=356mm, Ro=531mm, W=515rpm   R.D. STASTKA   7-22-83

THEORETICAL VELOCITY PROFILE
OUTER-CENTRAL REGION BDRY, R/Ro=0.9016
INNER-CENTRAL REGION BDRY, R/Ro=0.7915
INNER CYLINDER BOUNDARY
OUTER CYLINDER BOUNDARY

RADIAL POSITION, R/Ro
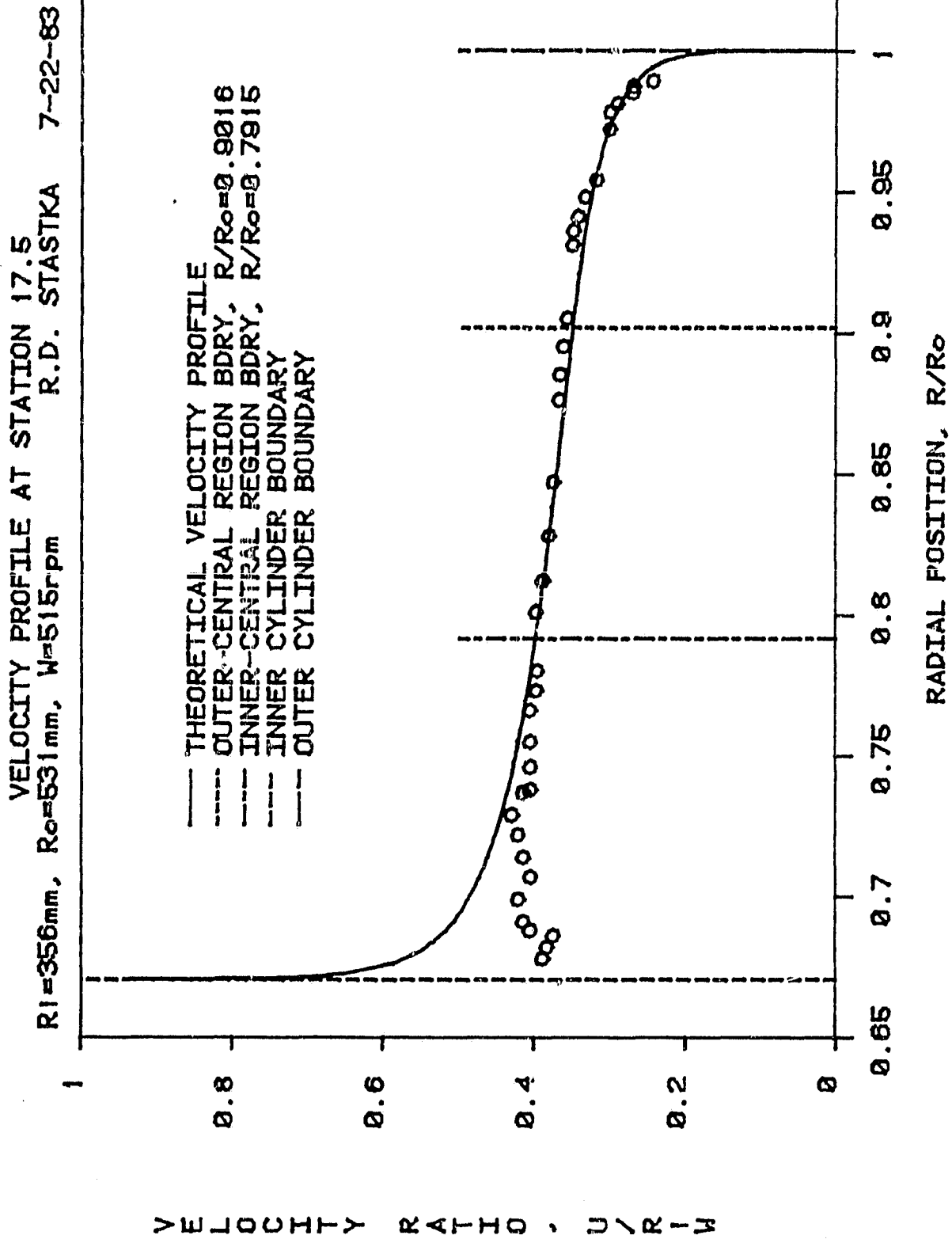
VELOCITY RATIO, U/R-W

FIGURE 11

VELOCITY PROFILE AT STATION 39.5
R.D. STASTKA   7-22-83
R1=356mm, Ro=531mm, W=515rpm

THEORETICAL VELOCITY PROFILE
OUTER-CENTRAL REGION BDRY, R/Ro=0.9015
INNER-CENTRAL REGION BDRY, R/Ro=0.7941
INNER CYLINDER BOUNDARY
OUTER CYLINDER BOUNDARY
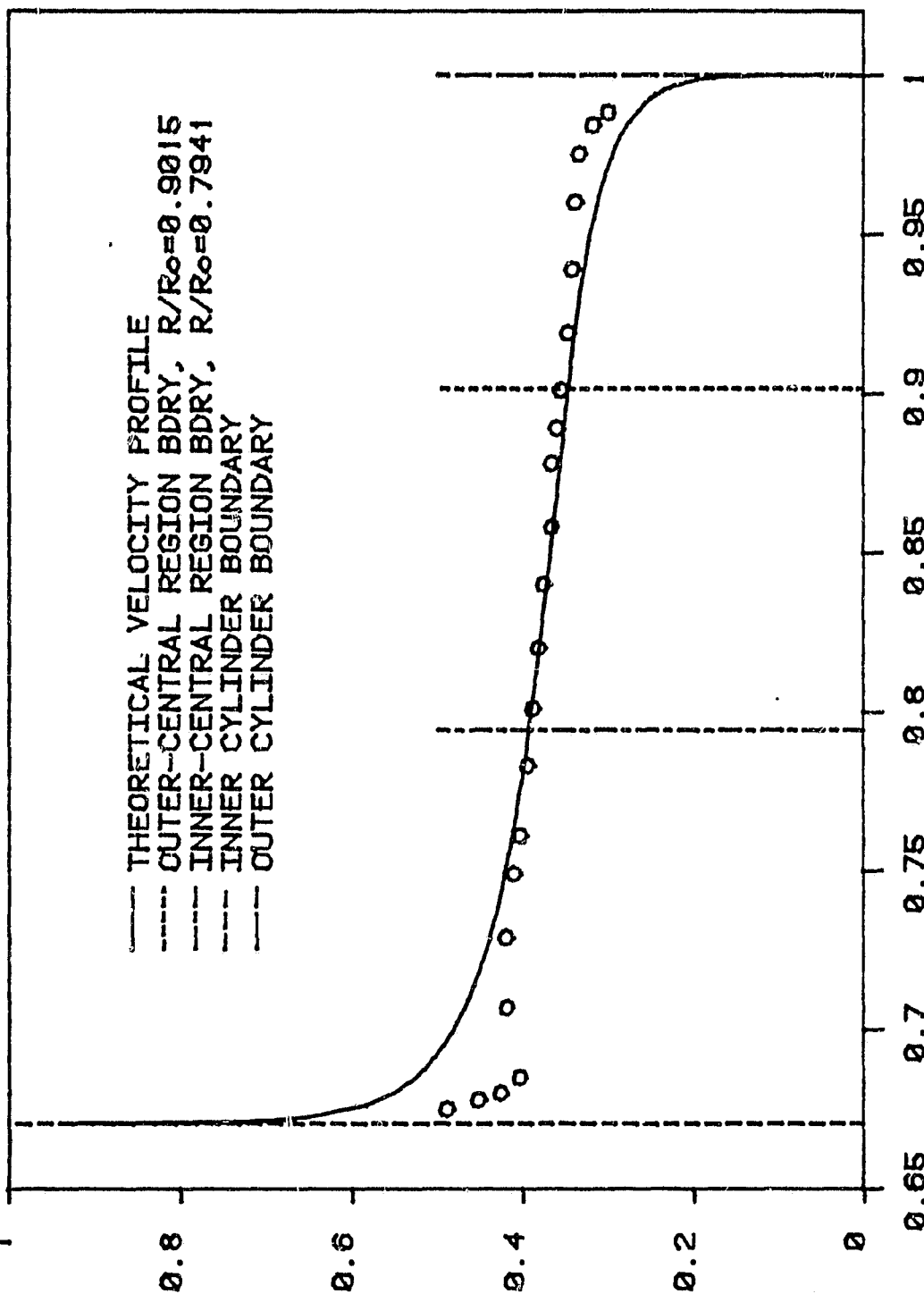
RADIAL POSITION, R/Ro

VELOCITY RATIO, U/R-W

FIGURE 12

VELOCITY PROFILE AT STATION 77.5
R.D. STASTKA   7-22-83

R1=356mm, Ro=531mm, W=515rpm

— THEORETICAL VELOCITY PROFILE
----- OUTER-CENTRAL REGION BDRY, R/Ro=0.9015
----- INNER-CENTRAL REGION BDRY, R/Ro=0.7842
--- INNER CYLINDER BOUNDARY
--- OUTER CYLINDER BOUNDARY

RADIAL POSITION, R/Ro
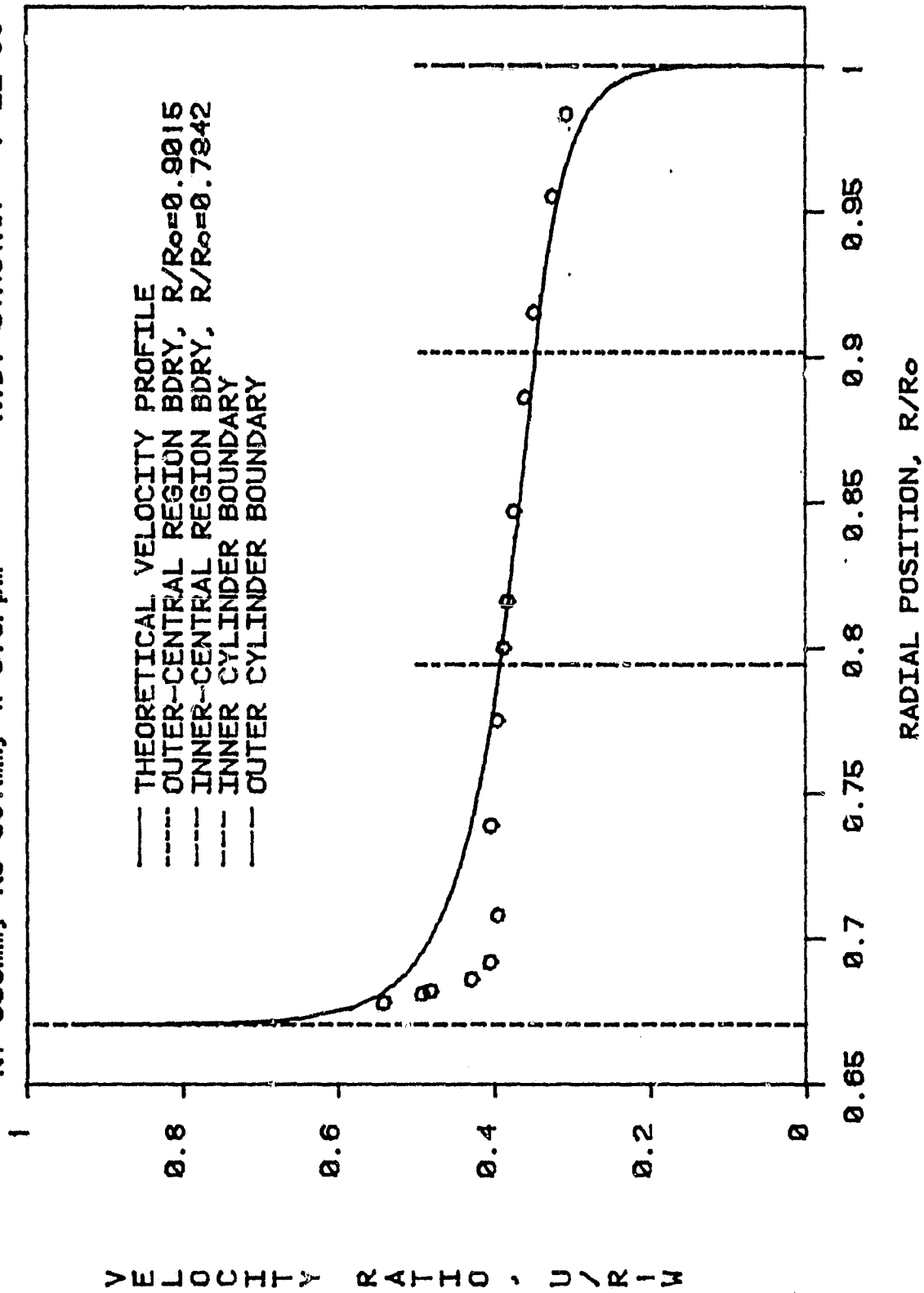
VELOCITY RATIO, U/R-W

FIGURE 13

VELOCITY PROFILE AT STATION 126.5   7-22-83
R.D. STASTKA
R1=356mm, Ro=531mm, W=515rpm
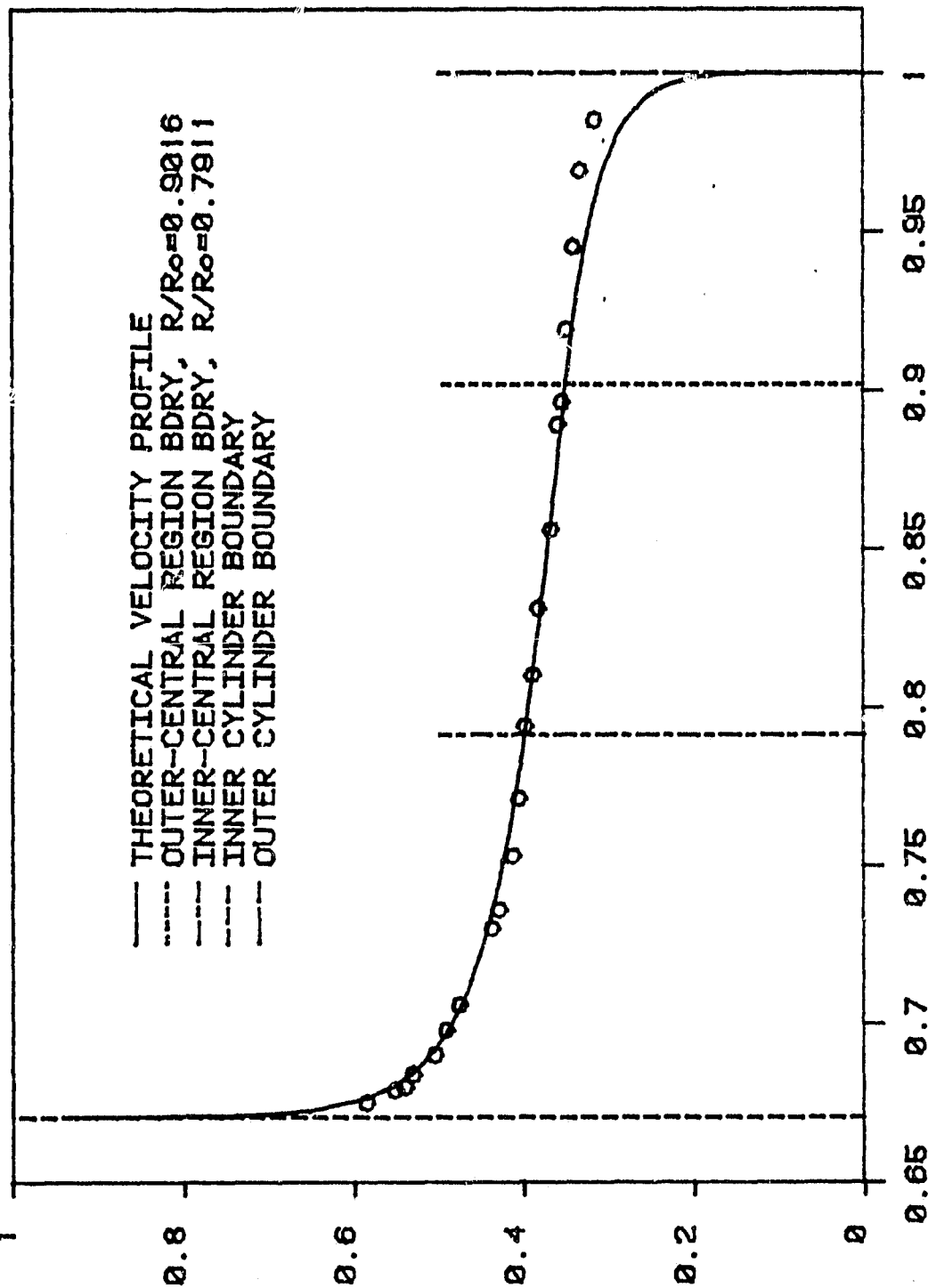
THEORETICAL VELOCITY PROFILE
OUTER-CENTRAL REGION BDRY, R/Ro=0.9016
INNER-CENTRAL REGION BDRY, R/Ro=0.7911
INNER CYLINDER BOUNDARY
OUTER CYLINDER BOUNDARY

RADIAL POSITION, R/Rō

VELOCITY RATIO, U/R-W

FIGURE 14

COMPARISON OF VELOCITY PROFILES AT DIFFERENT STATIONS
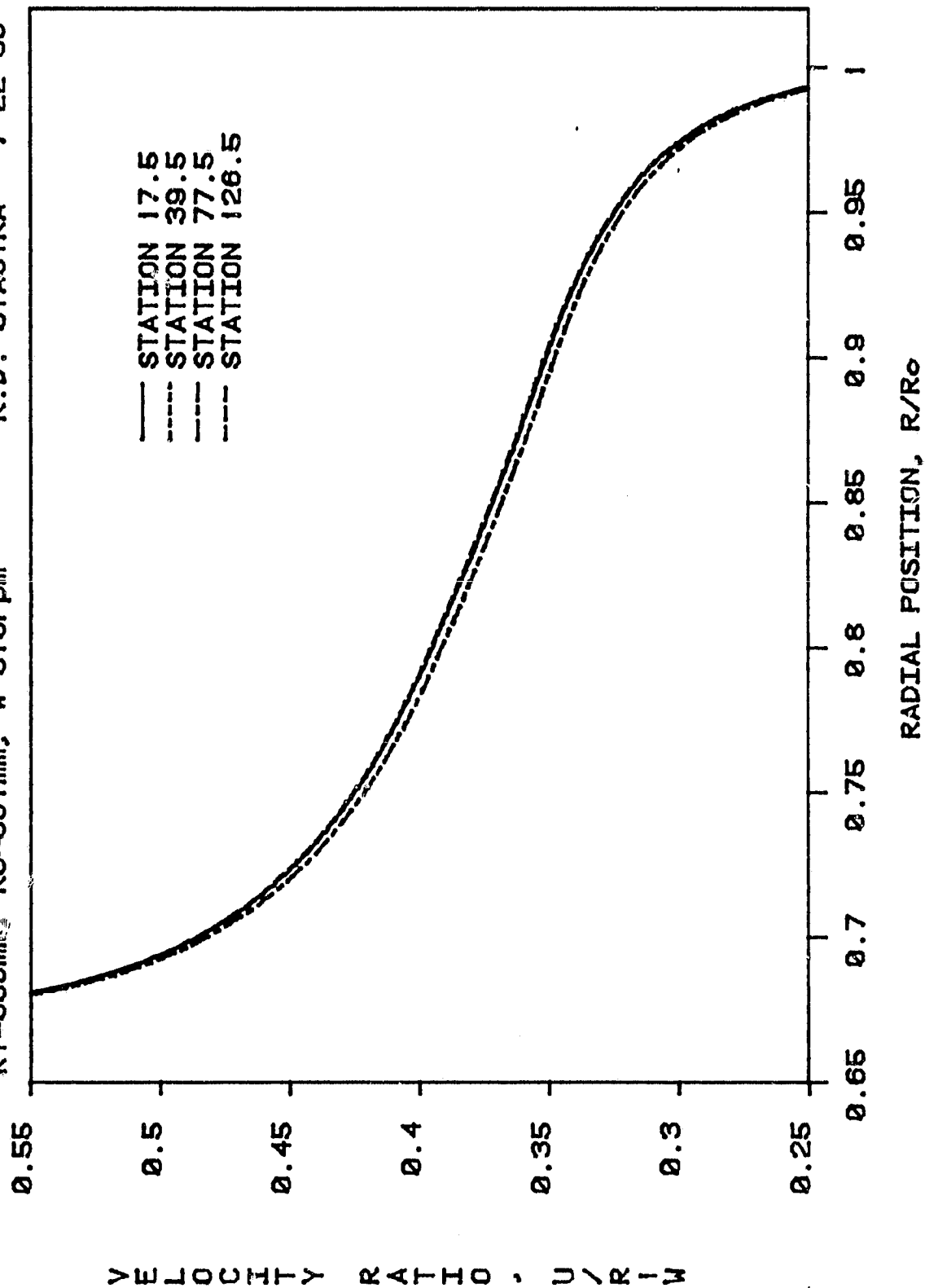R1=356mm, Ro=531mm, W=515rpm   R.D. STASTKA   7-22-83

STATION 17.5
STATION 39.5
STATION 77.5
STATION 126.5

RADIAL POSITION, R/Ro

VELOCITY RATIO, U/R-W
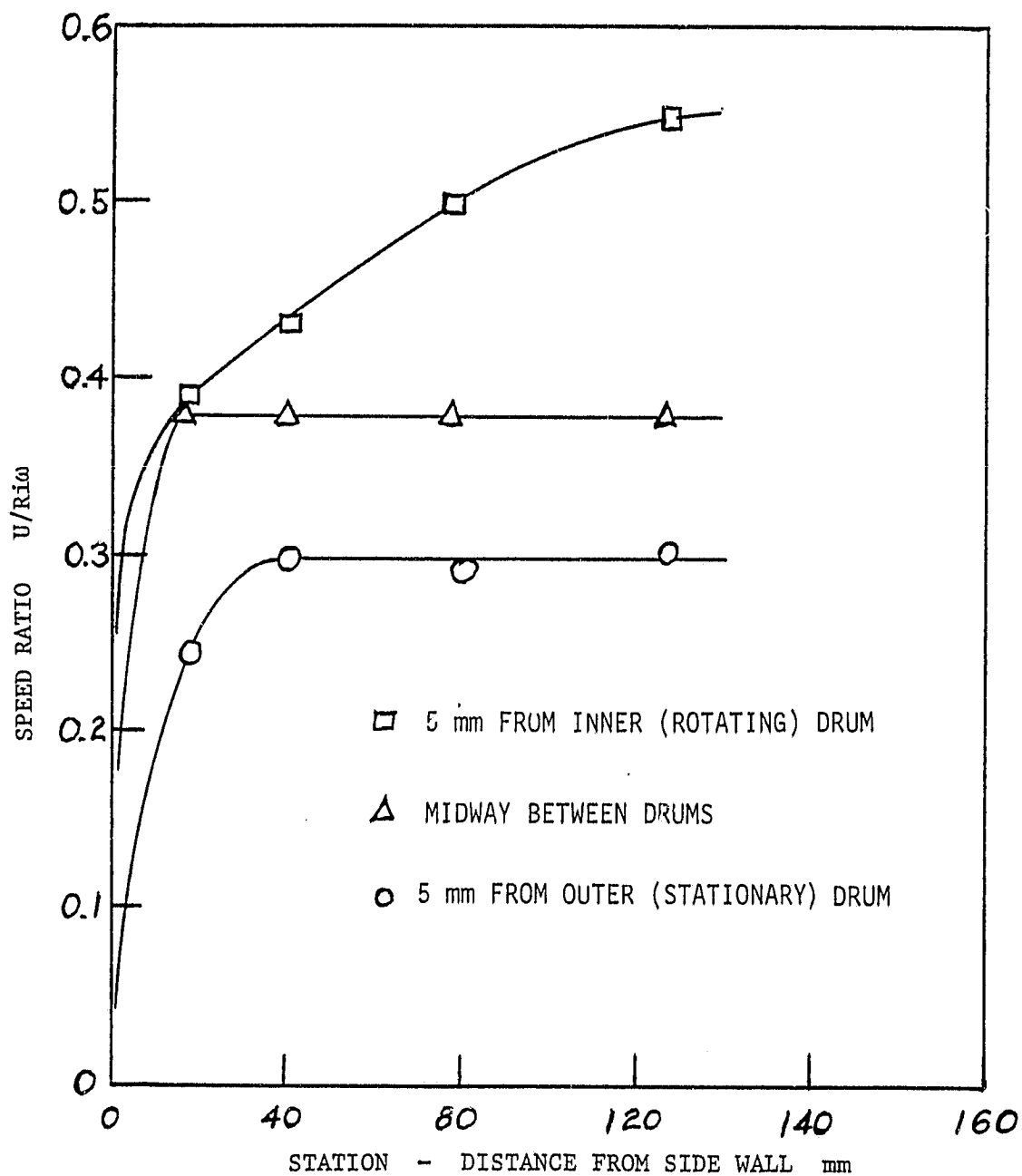
FIGURE 15

FIGURE 16

PARTICLE TRAJECTORY RELATIVE TO LAUNCH POINT IN A ZERO-G
VACUUM ENVIRONMENT
R.D. STASTKA   5-26-83

CYLINDER
$V_r = 0.2\ V_t$
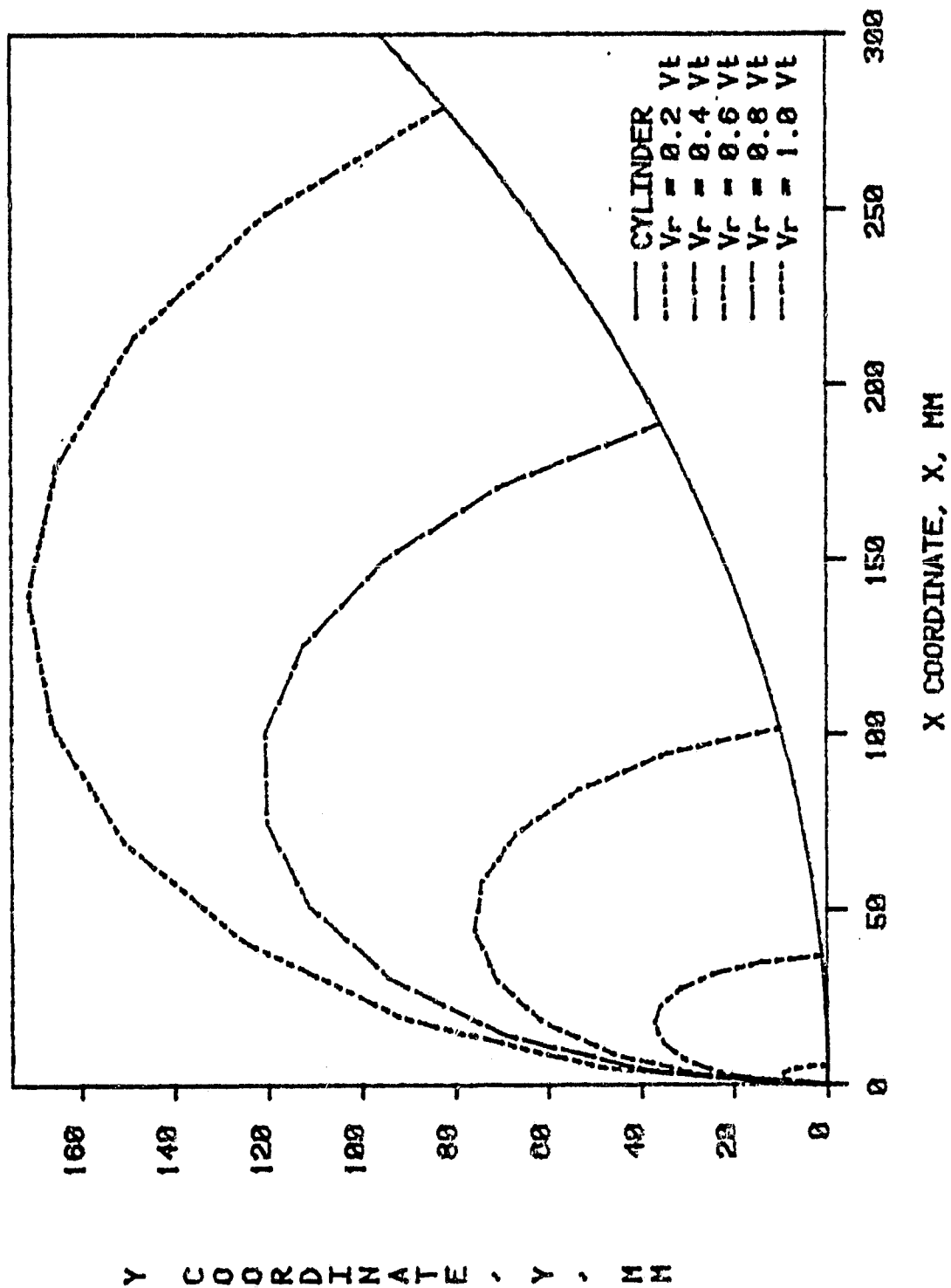$V_r = 0.4\ V_t$
$V_r = 0.6\ V_t$
$V_r = 0.8\ V_t$
$V_r = 1.0\ V_t$

X COORDINATE, X, MM

Y COORDINATE, Y, MM

FIGURE 17

PARTICLE TRAJECTORY IN ZERO-G SPACE CARROUSEL
DIAP=8.1mm, RI=347mm, Ro=517mm, W=515rpm STASTKA 8-18-83

PARTICLE TRAJECTORY
CYLINDER BOUNDARY

HORIZONTAL POSITION, X, MM

VERTICAL POSITION, Y, MM
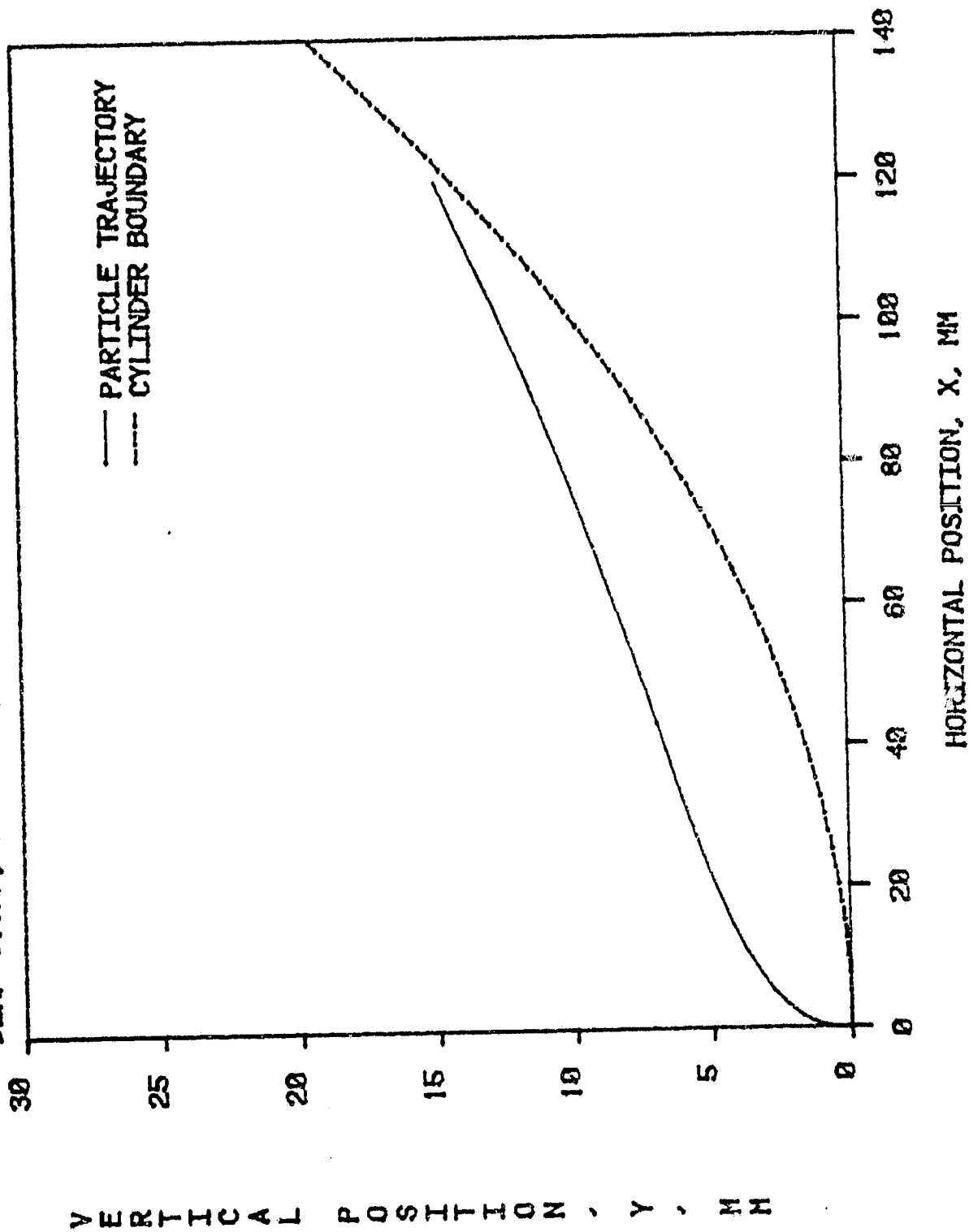
FIGURE 18

THEORETICAL VELOCITY PROFILE FOR TWO CONCENTRIC CYLINDERS
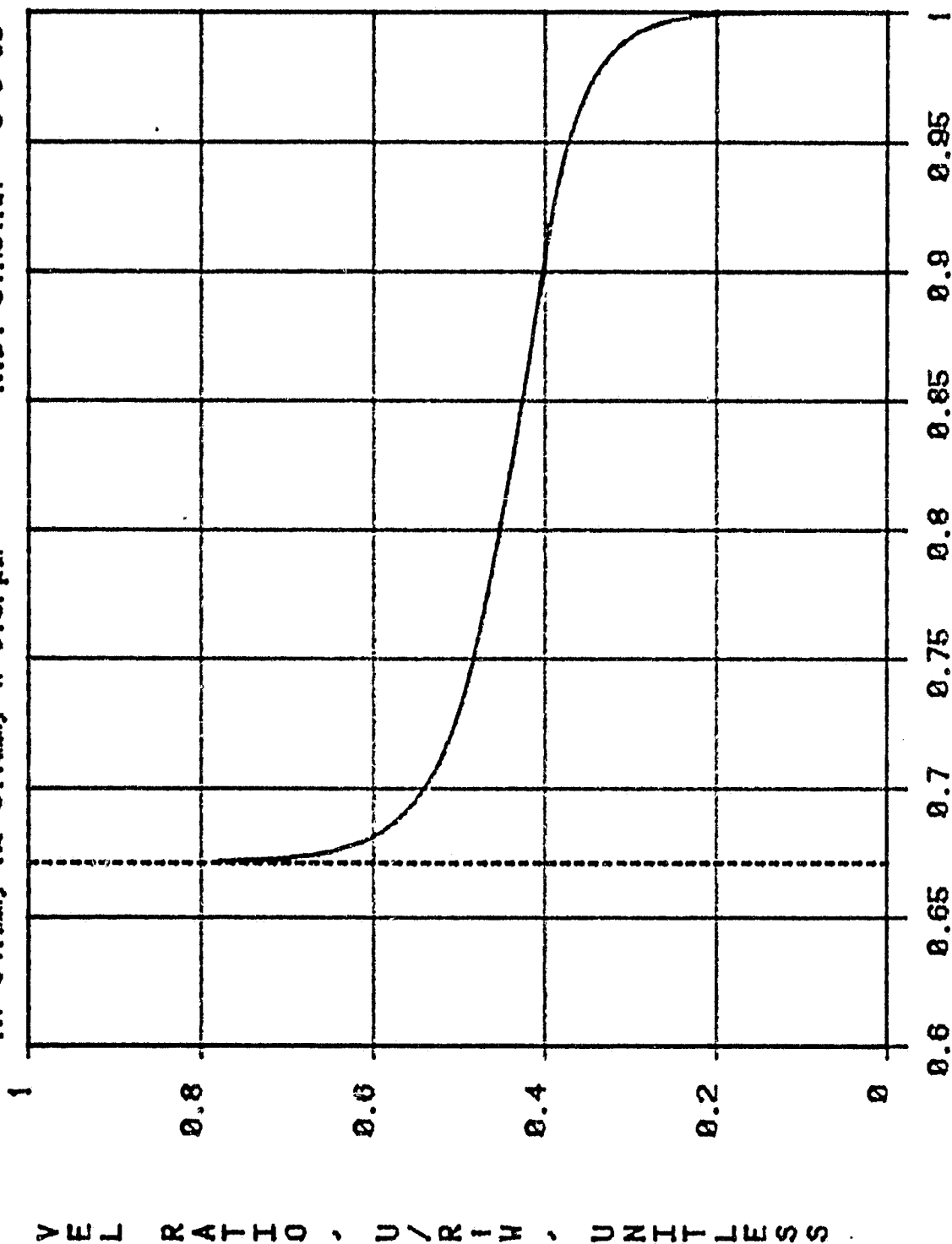Ri=347mm, Ro=517mm, W=515rpm   R.D. STASTKA   6-8-83

LOCATION, R/Ro, DIMENSIONLESS

VEL RATIO, U/RH, UNITLESS

FIGURE 19

R.D. STASTKA

PARTICLE TRAJECTORY COMPARISON

6-13-83
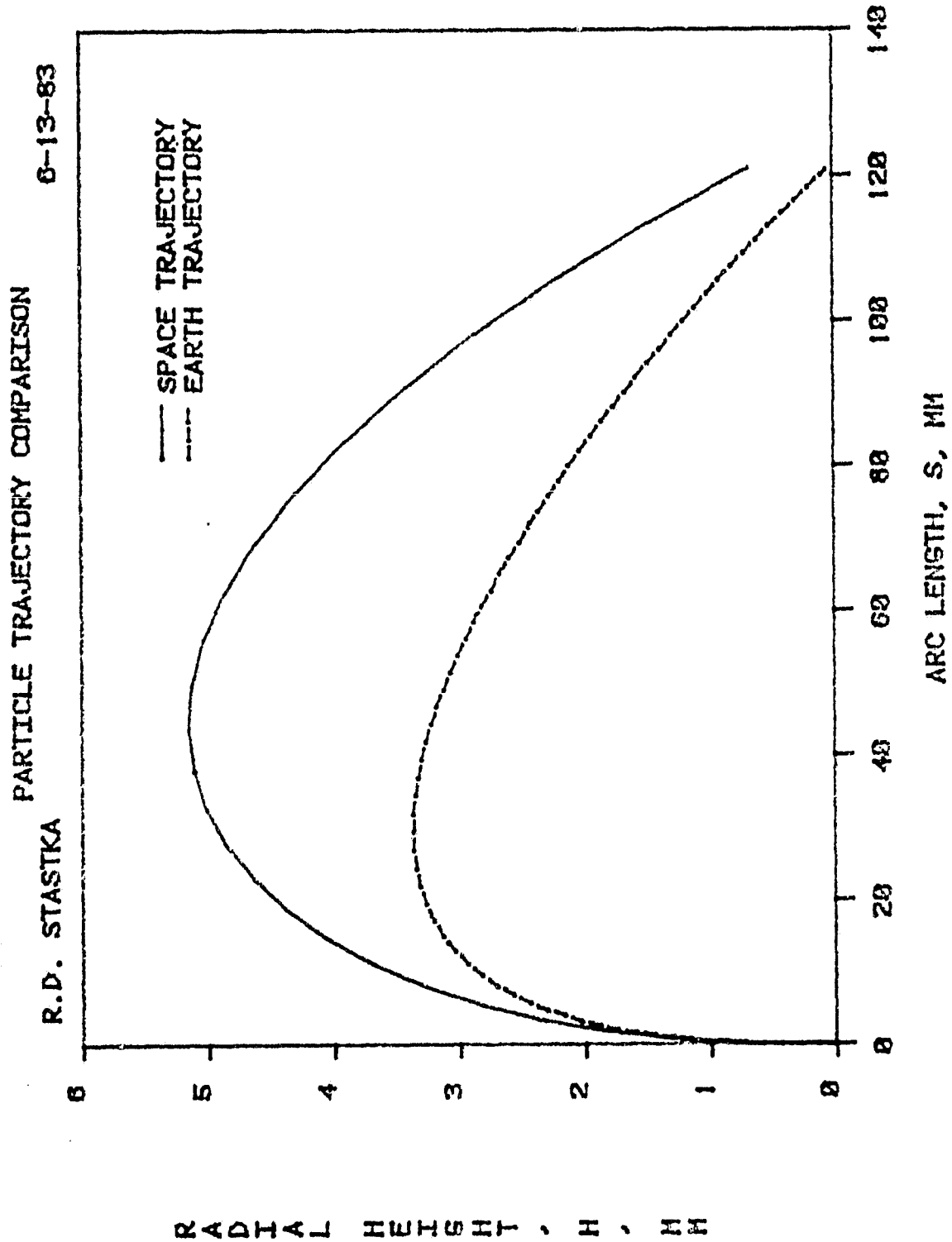
FIGURE 20

PARTICLE TRAJECTORY WITH 1 EARTH G IN SPACE CARROUSEL
DIAP=0.1mm, RI=347mm, Ro=517mm, N=515rpm STASTKA 6-12-83

——— PARTICLE TRAJECTORY
- - - CYLINDER BOUNDARY

HORIZONTAL POSITION, X, MM

VERTICAL POSITION, Y, MM

FIGURE 21